Published OnlineFirst September 25, 2020; DOI: 10.1158/2159-8290.CD-20-0336

RESEARCH ARTICLE

An Epigenetic Mechanism Underlying Chromosome 17p Deletion–Driven Tumorigenesis

Mei Chen[1], Xuelan Chen[1], Shujun Li[1], Xiangyu Pan[1], Yanqiu Gong[2], Jianan Zheng[1], Jing Xu[1], Chengjian Zhao[1], Qi Zhang[1], Shan Zhang[1], Lu Qi[1], Zhongwang Wang[1], Kaidou Shi[1], Bi-Sen Ding[3], Zhihong Xue[3], Lu Chen[3], Shengyong Yang[1], Yuan Wang[1], Ting Niu[1], Lunzhi Dai[2], Scott W. Lowe[4,5], Chong Chen[1], and Yu Liu[1]

ABSTRACT

Chromosome copy-number variations are a hallmark of cancer. Among them, the prevalent chromosome 17p deletions are associated with poor prognosis and can promote tumorigenesis more than *TP53* loss. Here, we use multiple functional genetic strategies and identify a new 17p tumor suppressor gene (TSG), plant homeodomain finger protein 23 (*PHF23*). Its deficiency impairs B-cell differentiation and promotes immature B-lymphoblastic malignancy. Mechanistically, we demonstrate that PHF23, an H3K4me3 reader, directly binds the SIN3–HDAC complex through its *N*-terminus and represses its deacetylation activity on H3K27ac. Thus, the PHF23–SIN3–HDAC (PSH) complex coordinates these two major active histone markers for the activation of downstream TSGs and differentiation-related genes. Furthermore, dysregulation of the PSH complex is essential for the development and maintenance of *PHF23*-deficient and 17p-deleted tumors. Hence, our study reveals a novel epigenetic regulatory mechanism that contributes to the pathology of 17p-deleted cancers and suggests a susceptibility in this disease.

SIGNIFICANCE: We identify *PHF23*, encoding an H3K4me3 reader, as a new TSG on chromosome 17p, which is frequently deleted in human cancers. Mechanistically, PHF23 forms a previously unreported histone-modifying complex, the PSH complex, which regulates gene activation through a synergistic link between H3K4me3 and H3K27ac.

Illustration by Bianca Dunn

[1]Department of Hematology and Institute of Hematology, State Key Laboratory of Biotherapy and Cancer Center, West China Hospital, Sichuan University, Chengdu, Sichuan, China. [2]Department of General Practice and National Clinical Research Center for Geriatrics, State Key Laboratory of Biotherapy, West China Hospital, Sichuan University, Chengdu, Sichuan, China. [3]Key Laboratory of Birth Defects and Related Diseases of Women and Children of MOE, State Key Laboratory of Biotherapy, West China Second University Hospital, Sichuan University, Chengdu, Sichuan, China. [4]Cancer Biology and Genetics Program, Memorial Sloan Kettering Cancer Center, New York, New York. [5]Howard Hughes Medical Institute, New York, New York.

Note: Supplementary data for this article are available at Cancer Discovery Online (http://cancerdiscovery.aacrjournals.org/).

M. Chen and X. Chen contributed equally to this work.

Corresponding Authors: Chong Chen, State Key Laboratory of Biotherapy, West China Hospital, Sichuan University, 17 Renming Road S3, Chengdu, Sichuan, China. Phone: 86 18980606532; E-mail: chongchen@scu.edu.cn; and Yu Liu, State Key Laboratory of Biotherapy, West China Hospital, Sichuan University, 17 Renming Road S3, Chengdu, Sichuan, China. Phone: 86 18980606672; E-mail: yuliuscu@scu.edu.cn

Cancer Discov 2021;11:1–14

doi: 10.1158/2159-8290.CD-20-0336

©2020 American Association for Cancer Research.

Downloaded from cancerdiscovery.aacrjournals.org on December 30, 2020. © 2020 American Association for Cancer Research.

Published OnlineFirst September 25, 2020; DOI: 10.1158/2159-8290.CD-20-0336

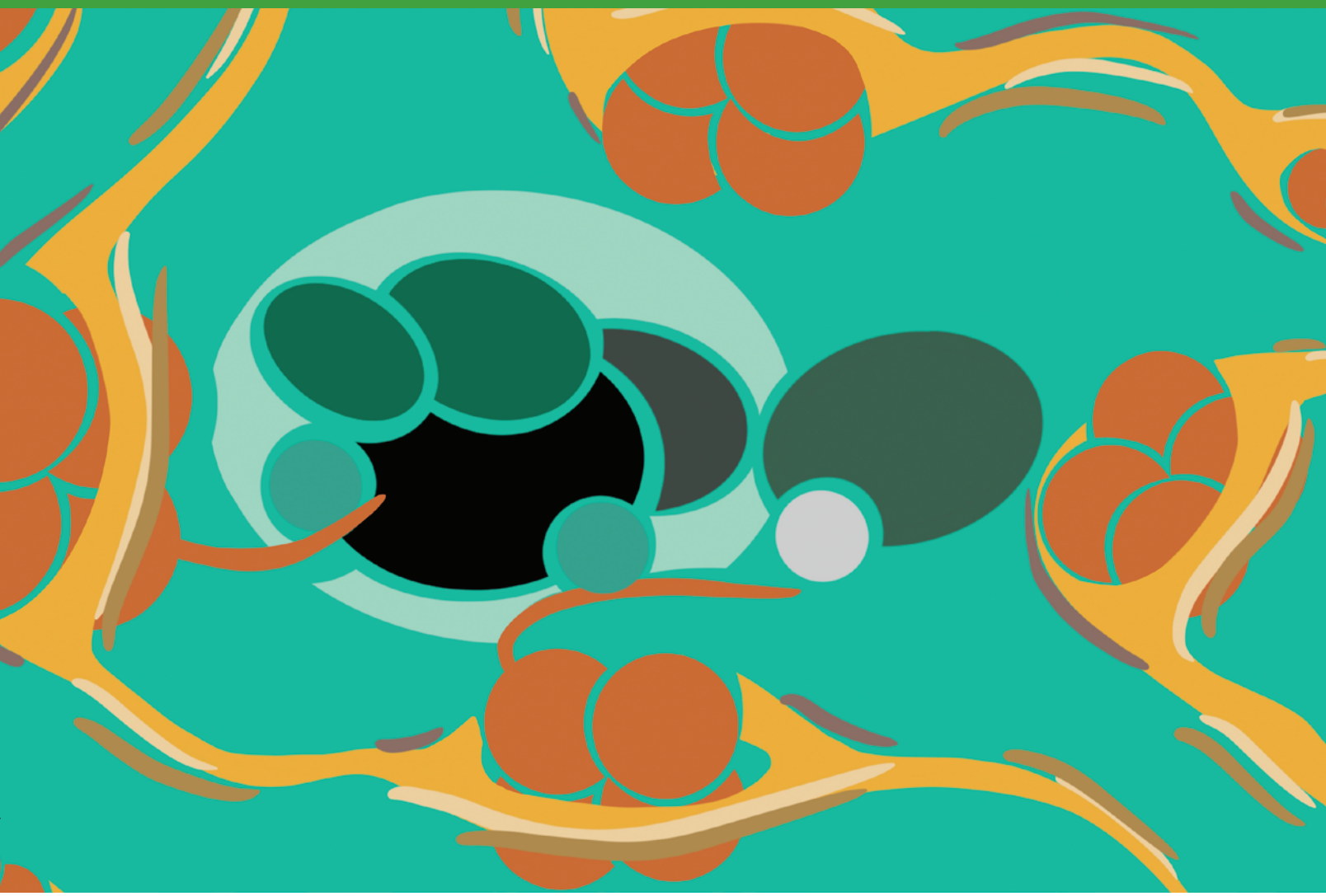

INTRODUCTION

Chromosome copy-number variations (CNV), which generally consist of hundreds or thousands of genes, are a common feature of human cancers (1, 2). Accumulating evidence indicates that specific CNVs are recurrent in many types of cancer, and some can occur at the early stages of tumorigenesis, suggesting that at least some cancer-associated CNVs may function as the drivers of human cancers (3, 4). For example, chromosome 3p deletions are detected in more than 90% of lung cancers, whereas chromosome 8q is frequently amplified in hepatocellular carcinoma (5, 6). Among them, heterozygous chromosome 17p deletions (del(17p)) are the most frequent chromosome loss in both solid cancers and hematopoietic malignancies, including lymphomas and leukemias (2–4, 7–10). It has been proposed that tumor suppressor genes (TSG) are enriched in cancer-associated chromosome deletion regions, whereas oncogenes are enriched in chromosome amplicons (11, 12). However, given that a large number of genes are involved in each CNV, it has been challenging to functionally identify potential TSGs and oncogenes for better mechanistic insights on CNVs in cancer. It had long been assumed that the only function of del(17p) is for *TP53* loss of heterozygosity, until our recent work (8). Using a conditional chromosome 11B3 (syntenic to human chromosome 17p13, a commonly deleted region in human cancers) deletion mouse model, we demonstrated that del(17p) could promote cancer development through both *TP53*-dependent and *TP53*-independent mechanisms. However, the additional TSGs in this region remain to be identified.

There are about 500 genes on chromosome 17p, and a large amount of effort has been made to identify new TSGs in this region (8, 13). According to the "two-hit" theory, most previous studies focused on searching for candidate TSGs with mutations/focal deletions in one allele and complete loss of the other allele through del(17p), similar to *TP53* (14). Unfortunately, limited success has been achieved with this strategy (15, 16). Most 17p genes involved in del(17p) remain intact in the other allele and are expressed in 17p-deleted cancers, although generally at reduced levels. Recently, it has been reported that *EIF5A* and *ALOX15B*, both located on chromosome 17p13.1, can prevent tumorigenesis by promoting apoptosis of premalignant B cells (8, 13). Interestingly, both *EIF5A* and *ALOX15B* are haploinsufficient TSGs, and neither

Downloaded from cancerdiscovery.aacrjournals.org on December 30, 2020. © 2020 American Association for Cancer Research.

Published OnlineFirst September 25, 2020; DOI: 10.1158/2159-8290.CD-20-0336

has a second hit on the other allele. These studies imply that potential TSGs involved in del(17p) have been largely underestimated and emphasize functional studies for further identifying TSGs within chromosome deletions.

In this study, we used our previous *in vivo* functional short hairpin RNA (shRNA) screening results (8) and analyzed the potential roles of plant homeodomain finger protein 23 (*PHF23*), located on chromosome 17p13.1, in immature B-lymphoblastic malignancy. As a putative epigenetic reader, the plant homeodomain (PHD) domain of PHF23 specifically binds to trimethylated lysine 4 of histone H3 (H3K4me3; refs. 17, 18). Interestingly, *PHF23* is reported to also be involved in recurrent chromosomal translocations, forming the oncofusion gene *NUP98–PHF23* in human acute myeloid leukemia (AML; refs. 17–20). *NUP98–PHF23* promotes leukemogenesis through its dysregulated chromatin-modifying activity. In contrast, in del(17p) cancer, one allele of *PHF23* is lost without recurrent mutations on the second allele, suggesting that its function may be lost in these cancers. It would be interesting to investigate whether and how an epigenetic reader involved in del(17p) plays a role in cancer biology.

RESULTS

PHF23 Is a 17p TSG

In our unbiased *in vivo* tumorigenesis screening with an shRNA library targeting genes on mouse chromosome 11B3, syntenic to human chromosome 17p13, the common deletion region of chromosome 17p, multiple shRNAs targeting *Phf23* were enriched in the resulting lymphomas/leukemias (ref. 8; Fig. 1A). By analyzing diffuse large B-cell lymphoma (DLBCL) cohorts from The Cancer Genome Atlas (TCGA), we found that *PHF23* expression was significantly reduced in DLBCLs with del(17p) compared with their counterparts, consistent with its DNA copy-number loss (Fig. 1B). Therefore, we hypothesized that *PHF23* might be a TSG on chromosome 17p.

To validate the role of *PHF23* in B-cell malignancies, we cointroduced multiple independent *Phf23* shRNAs (sh*Phf23.338*, sh*Phf23.877*, and sh*Phf23.971*) or control *Renilla* shRNA (sh*Ren*) with GFP and *Myc* into pre–B cells isolated from C57BL/6 mouse bone marrow (BM). These sh*Phf23* or sh*Ren* cells were then transplanted into sublethally irradiated congenic recipient mice (ref. 21; Supplementary Fig. S1). The recipient mice transplanted with sh*Phf23* cells developed tumors with enlarged lymph nodes, whereas none of the recipient mice with sh*Ren* did in the observation period (Fig. 1C and D). The median tumor onset times were 40 days for sh*Phf23.338*, 40 days for sh*Phf23.971*, and 53 days for sh*Phf23.877*, respectively. Flow cytometry analysis showed that all of the tumor cells were GFP positive, indicating that they originated from donor cells with sh*Phf23* (Fig. 1E). The expression of B-cell marker B220 and hematoxylin and eosin staining results indicated that these mouse tumors with sh*Phf23* displayed the characteristics of high-grade lymphoblastic lymphoma/leukemia (Fig. 1E and Supplementary Fig. S2A). The knockdown efficiencies of *Phf23* shRNAs in the resulting immature B-lymphoblastic malignant cells from enlarged lymph nodes of recipients were confirmed by qPCR and Western blotting (Fig. 1F and G).

To further confirm its tumor suppressor function, we designed single-guide RNAs (sgRNA) targeting the genomic DNA sequence encoding the PHD domain of PHF23, which recognizes and binds H3K4me3 (20). Fetal liver cells (FLC) enriched with hematopoietic stem and progenitor cells from E13.5 *Eμ–Myc* mouse embryos (22) were transduced with Cas9 and sgRNAs for *Phf23* (sg*Phf23*) or scramble sequence (sgScr) and then transplanted into sublethally irradiated congenic recipient mice (Supplementary Fig. S1). Whereas none of the sgScr recipients developed tumors during the observation period, six of eight sg*Phf23* recipient mice developed lymphoma/leukemia with a median tumor-free survival of 102 days (Fig. 1H and Supplementary Fig. S2B). sg*Phf23* generated loss-of-function mutations in the resulting lymphoma/leukemias, as shown by the T7E1 assay, Sanger sequencing of clonal lymphoma/leukemia, and Western blotting (Supplementary Fig. S2C–E).

To test whether our mouse lymphoma/leukemia model resembles human cancers with 17p deletions, we analyzed RNA-sequencing (RNA-seq) data of mouse lymphoma/leukemia cells with or without *Phf23* loss. Gene set enrichment analyses (GSEA) showed that genes upregulated in sh*Phf23* lymphoma/leukemia cells were significantly positively enriched in 17p-deleted human DLBCLs compared with those without 17p deletions [Normalized Enrichment Score (NES) = 1.75, FDR q = 0.00], whereas the downregulated genes in mouse sh*Phf23* lymphoma/leukemia cells were significantly negatively enriched in human DLBCLs with 17p deletions (NES = −1.39, FDR q = 0.02; Fig. 1I and J). These correlations suggested that our mouse lymphoma/leukemia with *Phf23* loss partially resembled human DLBCLs with 17p deletions, and *PHF23* was a key TSG on 17p. Thus, with both shRNA and CRISPR/Cas9-mediated genome-editing experiments, we identified *PHF23* as a TSG on chromosome 17p.

PHF23 Is a Haploinsufficient TSG and Cooperates with *TP53*

Chromosome 17p deletions usually occur as a heterozygous loss (3, 4, 23). TSGs on chromosome deletions presumably need loss of heterozygosity through various mechanisms, such as mutations, focal deletions, and epigenetic silencing during tumorigenesis (24). However, according to cBioPortal, mutations on *PHF23* were rare in human cancers (Supplementary Fig. S2F), and the expression of *PHF23* in patients with del(17p) DLBCL was significantly reduced compared with those with intact chromosome 17p (Fig. 1B). Similarly, some other genes involved in large chromosomal deletions, such as *MLL3* on chromosome 7q, have been shown to be haploinsufficient TSGs (12, 25, 26). Hence, we hypothesized that *PHF23* might also be a haploinsufficient TSG on chromosome 17p. Consistently, although the expression levels of *Phf23* were significantly reduced, there were remarkable remaining *Phf23* mRNA and protein in sh*Phf23* lymphoma/leukemia (Fig. 1F and G). Heterozygous mutations of *Phf23* were also detected in sg*Phf23* lymphoma/leukemia (Supplementary Fig. S2D).

To test this hypothesis, we generated *Phf23* knockout mice with CRISPR/Cas9 editing, which resulted in a 14-bp insertion on exon 5 and a presumable premature stop codon (Fig. 2A and B). *Phf23*$^{-/-}$ mice were embryonically lethal

Downloaded from cancerdiscovery.aacrjournals.org on December 30, 2020. © 2020 American Association for Cancer Research.

Published OnlineFirst September 25, 2020; DOI: 10.1158/2159-8290.CD-20-0336

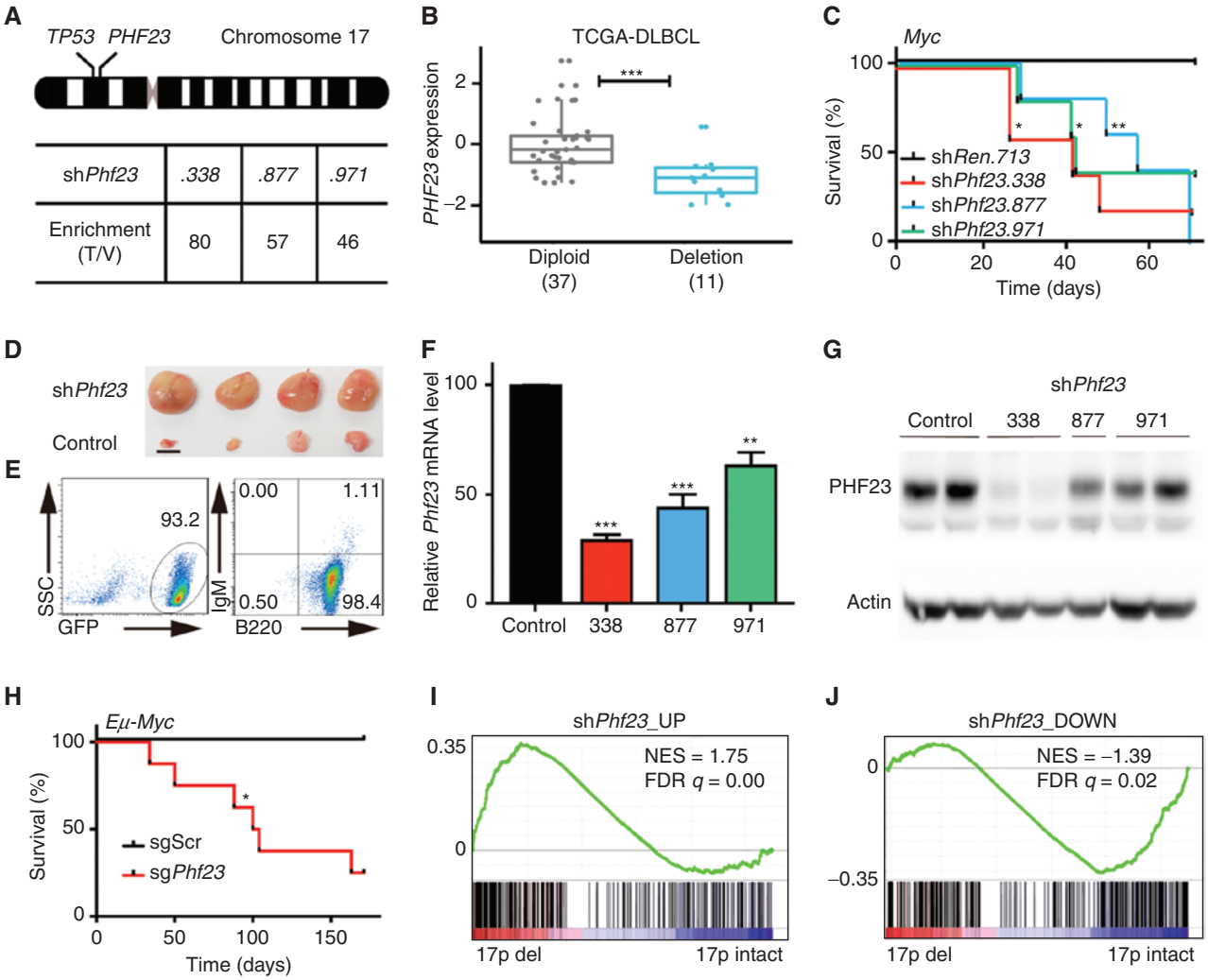

Figure 1. *Phf23* deficiency promotes lymphomagenesis. **A,** Top, a schematic diagram of human chromosome 17, showing the relative positions of *TP53* and *PHF23* on 17p. Bottom, the enrichment folds of *Phf23* shRNAs in the shRNA library screening of mouse chromosome 11B3 genes in MYC-driven lymphoma/leukemia in mice. The enrichment folds were calculated by dividing the percentages of each shRNA read in tumors by those in the library of plasmids. **B,** The expression levels of *PHF23* in patients with DLBCL with (deletion) or without (diploid) chromosome 17p deletions. RNA-seq data with RNA-seq by Expectation Maximization (RSEM) were analyzed from TCGA. ***, $P_{adj} < 0.001$, Wilcoxon signed-rank test. **C,** Kaplan–Meier tumor-free survival curves of recipient mice transplanted with pre-B cells infected with *Myc* cDNA and indicated shRNAs. $n = 5$ for each group. *, $P < 0.05$; **, $P < 0.01$ (log-rank test). **D,** Representative picture showing enlarged lymph nodes in recipient mice with sh*Phf23*. Scale bar, 5 mm. **E,** Representative flow plots showing the expression of GFP, B220, and IgM of sh*Phf23* lymphoma/leukemia cells. **F,** Relative expression levels of *Phf23* in sh*Phf23* lymphoma/leukemia cells, measured by qPCR. Control, sh*Trp53;Myc* lymphoma/leukemia cells. **G,** Representative Western blotting picture showing the protein levels of PHF23 in sh*Phf23* lymphoma/leukemia cells. Control, sh*Trp53;Myc* lymphoma/leukemia cells. **H,** Kaplan–Meier tumor-free survival curves of recipient mice transplanted with *Eμ-Myc* FLCs with CRISPR/Cas9 targeting *Phf23* or scramble sequence. $n = 5$, sgScr; $n = 8$, sg*Phf23*. *, $P < 0.05$ (log-rank test). **I,** GSEA showing the positive enrichment of the sh*Phf23* lymphoma/leukemia upregulated gene set in 17p-deleted TCGA DLBCL compared with 17p intact ones (NES = 1.75; FDR $q = 0.00$). **J,** GSEA showing the negative enrichment of the sh*Phf23* lymphoma/leukemia downregulated gene set in 17p-deleted TCGA DLBCL compared with 17p intact ones (NES = −1.39; FDR $q = 0.02$).

(E15.5–16.5; unpublished data). Western blotting showed that the expression levels of PHF23 in FLCs from *Phf23*$^{+/-}$ embryos were precisely reduced to 50% of that in wild-type (WT), whereas they were completely lost in *Phf23*$^{-/-}$ cells (Fig. 2C). *Phf23* WT, heterozygous, and homozygous knockout FLCs were transduced with *Myc* cDNA, followed by transplantation into sublethally irradiated congenic recipient mice (Supplementary Fig. S1). Consistent with the aforementioned tumorigenesis experiments with shRNA and CRISPR/Cas9 (Fig. 1C and H), recipients transplanted with *Phf23*$^{-/-}$ FLCs transduced with *Myc* had significantly shorter tumor onset times than those with WT FLCs with *Myc* overexpression (Fig. 2D). Surprisingly, *Phf23*$^{+/-}$ FLCs also gave rise to tumors with a similar latency as *Phf23*$^{-/-}$ cells. Interestingly, *Myc*-overexpressing *Phf23*$^{+/+}$ FLCs led to typical myeloid leukemia, indicated by expression of myeloid lineage markers CD11b and Gr1 but not B220, consistent with a previous report (27). In contrast, recipient mice with both *Phf23*$^{-/-}$ and *Phf23*$^{+/-}$ cells had enlarged lymph nodes, and their tumor cells were B220^{+}CD11b^{-}Gr1^{-} (Fig. 2E and F). Therefore, *Phf23*

Downloaded from cancerdiscovery.aacrjournals.org on December 30, 2020. © 2020 American Association for Cancer Research.

Published OnlineFirst September 25, 2020; DOI: 10.1158/2159-8290.CD-20-0336

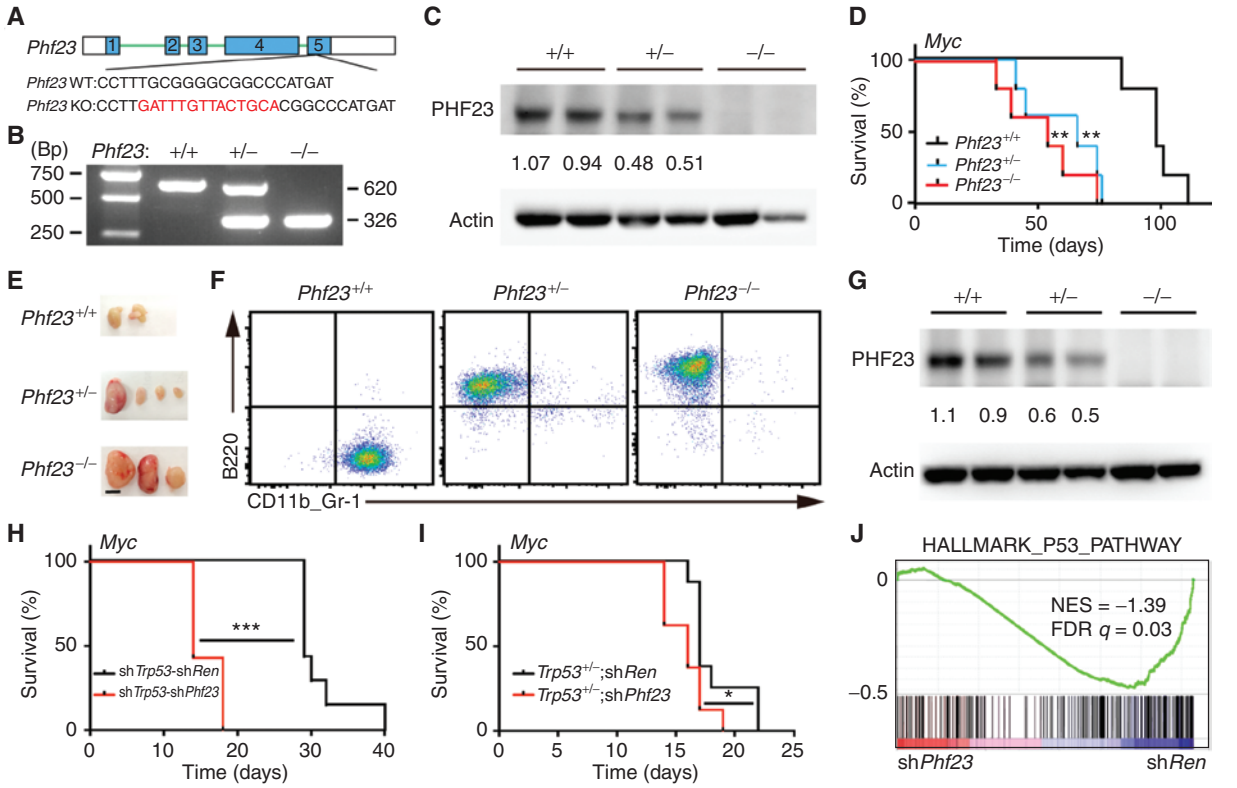

Figure 2. *PHF23* is a haploinsufficient TSG and cooperates with p53. **A,** Diagram showing *Phf23* mutation with a 14-bp insertion on one allele introduced by CRISPR/Cas9 in exon 5 in mice. **B,** Representative picture showing genotyping of $Phf23^{+/+}$, $Phf23^{+/-}$, and $Phf23^{-/-}$ mice. **C,** Representative Western blotting picture showing the protein levels of PHF23 in $Phf23^{+/+}$, $Phf23^{+/-}$, and $Phf23^{-/-}$ E14.5 FLCs. **D,** Kaplan–Meier tumor-free survival curves of recipient mice transplanted with *Myc*-transduced E14.5 FLCs derived from $Phf23^{+/+}$, $Phf23^{+/-}$, and $Phf23^{-/-}$ embryos. $n = 5$ for each group. **, $P < 0.01$ (log-rank test). **E,** Representative pictures showing enlarged lymph nodes in recipient mice with *Myc*-transduced $Phf23^{+/-}$ or $Phf23^{-/-}$ FLCs but not $Phf23^{+/+}$ FLCs in **D.** Scale bar, 5 mm. **F,** Representative flow plots showing the expression of B220 and CD11b/Gr1 in $Phf23^{+/+}$, $Phf23^{+/-}$, and $Phf23^{-/-}$ tumor cells from recipient mice in **D. G,** Western blotting of PHF23 in $Phf23^{+/+}$;*Myc*, $Phf23^{+/-}$;*Myc*, and $Phf23^{-/-}$;*Myc* lymphoma/leukemia cells from recipient mice in **D.** Note: $Phf23^{+/+}$;*Myc* lymphoma/leukemia cells had *Trp53* mutations by CRISPR/Cas9. **H,** Kaplan–Meier tumor-free survival curves of recipient mice transplanted with pre–B cells infected with *Myc*-linked tandem shRNAs. $n = 7$, ***, $P < 0.001$ (log-rank test). **I,** Kaplan–Meier tumor-free survival curves of recipient mice transplanted with $Trp53^{+/-}$ pre–B cells infected with *Myc*-linked sh*Ren* or sh*Phf23*. *, $P < 0.05$ (log-rank test). **J,** GSEA showing the negative enrichment of the HALLMARK_P53_PATHWAY gene set in sh*Phf23* lymphoma/leukemia cells compared with sh*Ren* cells (NES = –1.39; FDR $q = 0.03$).

heterozygosity, similar to *Phf23* null, promoted MYC-driven lymphoma/leukemia. To rule out the possibility of loss of heterozygosity of *Phf23* during $Phf23^{+/-}$ lymphomagenesis, we measured the protein levels of PHF23 in the resulting lymphoma/leukemia by Western blotting. The results showed that the protein levels of PHF23 in $Phf23^{+/-}$ lymphoma/leukemia remained at about half of that in $Phf23^{+/+}$ cells, indicating that the second allele of *Phf23* remained intact during lymphomagenesis (Fig. 2G). Moreover, the WT *Phf23* allele was confirmed to remain in the $Phf23^{+/-}$ tumor cells (data not shown). Altogether, these results strongly suggested that *PHF23* was a haploinsufficient TSG.

Codeleted TSGs within large chromosomal deletions have been suggested to be able to cooperate during tumorigenesis (8, 13). Here, we wondered whether *Phf23* deficiency would cooperate with *Trp53* loss, arguably the most important TSG on chromosome 17p, to promote lymphomagenesis. Although *Trp53* knockdown promoted MYC-driven immature B-lymphoblastic malignancy, co-knockdown of both *Trp53* and *Phf23* by shRNA (sh*Trp53*–sh*Phf23*) significantly shortened the latency from 29 days to 14 days (Fig. 2H). A similar cooperative effect between *Trp53* and *Phf23* deficiencies was observed with $Trp53^{+/-}$ pre-B cells (Fig. 2I). To explore the potential molecular mechanisms of the synergy of *Phf23* and *Trp53*, RNA-seq analyses of sh*Ren* and sh*Phf23* B-lymphoma/leukemia cells were performed. GSEA showed that the genes in the p53 pathway were significantly negatively enriched in *Phf23*-deficient tumor cells compared with sh*Ren* cells (Fig. 2J). Hence, loss of *PHF23* and *TP53* through 17p deletions may cooperate to drive tumorigenesis through synergistic repressions of the p53 pathway.

PHF23 Colocalizes with H3K4me3 on Gene Promoters and Is Required for B-cell Differentiation

PHF23 contains a PHD domain at its C-terminus, which has been shown to specifically bind H3K4me3 (20). In NUP98–PHF23 fusion–driven AML, NUP98–PHF23 binds a specific subset of H3K4me3 and regulates the expression of multiple AML-associated genes (18, 28). Here, we studied the functions

Downloaded from cancerdiscovery.aacrjournals.org on December 30, 2020. © 2020 American Association for Cancer Research.

Published OnlineFirst September 25, 2020; DOI: 10.1158/2159-8290.CD-20-0336

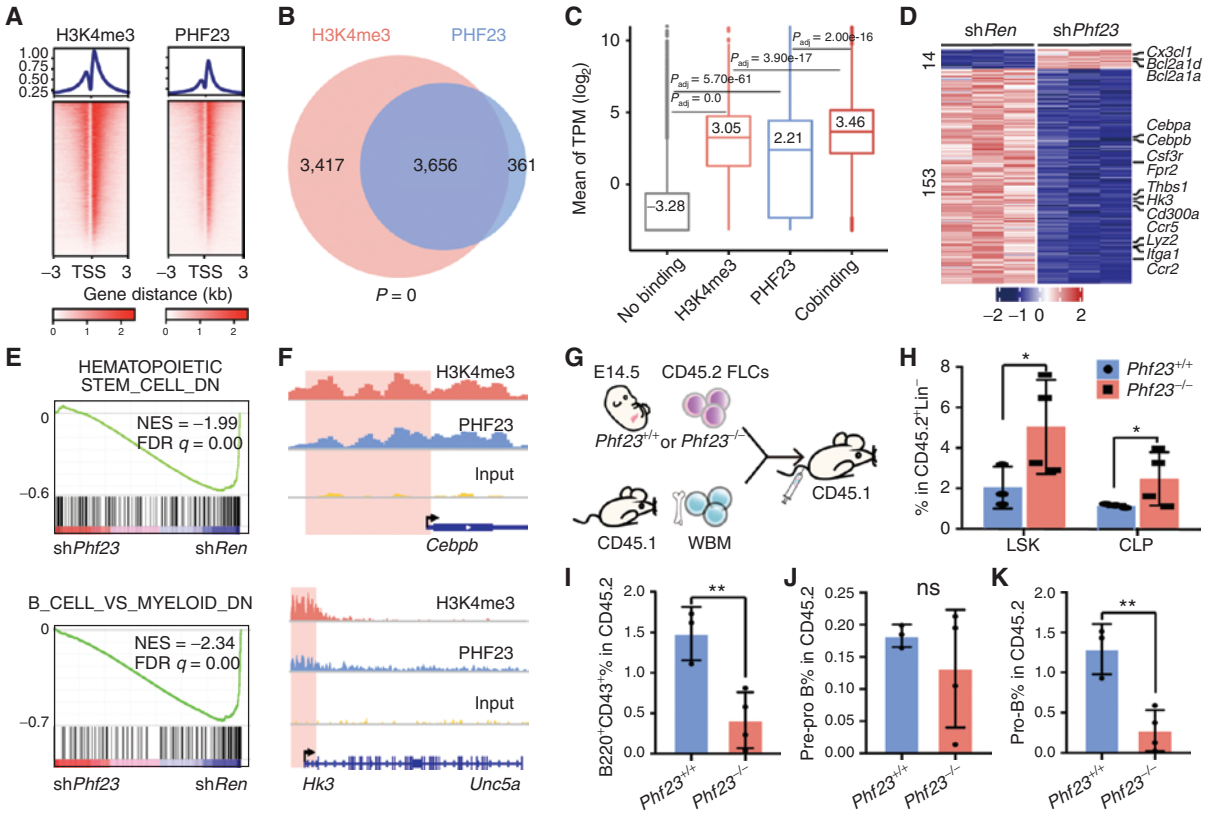

Figure 3. PHF23 colocalizes with H3K4me3 in pre-B cells and is required for B-cell differentiation. **A,** Top, profiles showing average H3K4me3 (left) and PHF23 (right) bound peak densities in TSS regions by ChIP-seq analyses. Bottom, heat maps showing H3K4me3 and PHF23 bound peaks in TSS regions. **B,** Venn diagram showing overlapping of PHF23 and H3K4me3 bound genes; *P*, Fisher exact test. **C,** Mean $\log_2$ TPM of genes with no binding (without H3K4me3 and PHF23 binding), H3K4me3 only, PHF23 only, or cobinding (have H3K4me3 and PHF23 binding) in Ba/F3 cells. P_{adj}, Wilcoxon signed-rank test. **D,** Heat map showing the differentially expressed genes ($P_{adj} < 0.05$, $\log_2$ fold change >1 or <−1) in sh*Phf23* pre-B cells compared with those with sh*Ren*. **E,** GSEA showing the negative enrichments of the HEMATOPOIETIC_STEM_CELL_DOWN (NES = −1.99; FDR $q = 0.00$) and B_CELL_VS_MYELOID_DOWN gene sets (NES = −2.34; FDR $q = 0.00$) in sh*Phf23* pre-B cells compared with sh*Ren* cells. **F,** Integrative Genomics Viewer (IGV) showing binding peaks of H3K4me3 and PHF23 on *Cebpb* (top) and *Hk3* (bottom). **G,** Schematic diagram of the hematopoiesis analyses of *Phf23*$^{+/+}$ and *Phf23*$^{-/-}$ FLCs. **H,** Percentages of donor-type LSK ($Lin^-Sca1^+cKit^+$) and CLP ($Lin^-Sca1^{lo}cKit^{lo}$) populations in the bone marrow of recipient mice 4 months after bone marrow transplant. **I,** Percentages of donor-type $B220^+CD43^+$ populations in the bone marrow of recipient mice. **J,** Percentages of donor-type $B220^+CD43^+CD24^-$ (pre/pro-B) populations in the bone marrow of recipient mice. **K,** Percentages of donor-type $B220^+CD43^+$ $CD24^+$ (pro-B) populations in the bone marrow of recipient mice. **H–K,** *, $P < 0.05$; **, $P < 0.01$; ns, not significant (*t* test).

of WT PHF23 in Ba/F3 cells, a mouse pro/pre-B-cell line (29), by chromatin immunoprecipitation–sequencing (ChIP-seq) assay. We found that most (>70%) PHF23 binding sites were located in gene promoters with a similar pattern as H3K4me3 peaks (Fig. 3A and Supplementary Fig. S3A). More than 90% of PHF23 binding peaks overlapped with H3K4me3 peaks (Fig. 3B). H3K4me3 is commonly enriched on active promoters (30), and consistently the average expression levels of H3K4me3 binding genes were significantly higher than those without binding in Ba/F3 cells (ref. 31; Fig. 3C). Interestingly, PHF23 binding was associated with further mildly but significantly increased expression of genes [average $\log_2$ transcripts per kilobase million (TPM) of genes with both PHF23 and H3K4me3 binding versus with only H3K4me3 binding: 3.46 versus 3.05, P_{adj} = 3.90e−17; those with only PHF23 binding versus without binding: 2.21 versus −3.28, P_{adj} = 5.70e-61; Fig. 3C]. A similar gene expression pattern was also observed in freshly isolated pre–B cells (Supplementary Fig. S3B). Thus, PHF23 colocalized with H3K4me3 and regulated gene activation.

Accordingly, there were more significantly downregulated genes than upregulated ones (153 vs. 14) in *Phf23* knockdown pre–B cells compared with those in sh*Ren* cells (Fig. 3D and Supplementary Table S1). Consistent with the tumor suppression function of PHF23, upregulated genes in sh*Phf23* cells were enriched in pathways of cell survival and proliferation, such as negative regulation of apoptosis signaling pathway and positive regulation of ERK1 and ERK2 cascade, whereas the downregulated genes were enriched in pathways related to leukocyte differentiation and functions, suggesting potential roles of PHF23 in hematopoiesis (Supplementary Fig. S3C and D). GSEA showed that the HEMATOPOIETIC_STEM_CELL_DOWN gene set and B_CELL_VS_MYELOID_DOWN gene set were significantly negatively enriched in sh*Phf23* cells (NES = −1.99 and −2.34; FDR $q = 0.00$ and 0.00, respectively; Fig. 3E). Among the most downregulated genes, *Cebpb* and *Hk3* have been shown to be important for B-cell development and function (refs. 32, 33; Fig. 3F). Interestingly, the genes bound by PHF23 were significantly overlapped with those by NUP98–PHF23 (ref. 18; Supplementary

Downloaded from cancerdiscovery.aacrjournals.org on December 30, 2020. © 2020 American Association for Cancer Research.

Published OnlineFirst September 25, 2020; DOI: 10.1158/2159-8290.CD-20-0336

Fig. S3E). The overlapped genes included the well-known tumor suppressor genes *Cdkn1b, Cdkn2c, Nf1*, and *Fbxw7*. These data suggested that PHF23 was required for the expression of tumor suppressor and differentiation-related genes.

To directly test the function of *Phf23* in B-cell development, we transplanted *Phf23*$^{+/+}$ or *Phf23*$^{-/-}$ hematopoietic stem and progenitor cells together with recipient-type BM cells for irradiation protection into lethally irradiated recipient mice. Given that the *Phf23*$^{-/-}$ mice were embryonically lethal, *Phf23*$^{+/+}$ or *Phf23*$^{-/-}$ FLCs were used (Fig. 3G). Four months later, the donor-type BM cells were analyzed. The percentages of both hematopoietic stem and progenitor cells [Lin$^-$Sca1$^+$cKit$^+$ (LSK)] and common lymphoid progenitor cells (CLP; Lin$^-$Sca1^{lo}cKit^{lo}) were significantly increased in the BM of recipient mice with *Phf23*$^{-/-}$ FLCs compared with those with *Phf23*$^{+/+}$ FLCs (Fig. 3H and Supplementary Fig. S4A). However, the B-progenitor cells (B220$^+$CD43$^+$) were significantly less in recipients with *Phf23*$^{-/-}$ FLCs than those with *Phf23*$^{+/+}$ FLCs (Fig. 3I and Supplementary Fig. S4B). In more detail, the *Phf23*$^{-/-}$ pre/pro–B cells (B220$^+$CD43$^+$CD24$^-$) were comparable to WT, whereas the pro–B cells (B220$^+$CD43$^+$CD24$^+$) were significantly reduced in recipients (1.2% versus 0.2%) with *Phf23*$^{-/-}$ FLCs compared with those with WT FLCs (Fig. 3J and K and Supplementary Fig. S4C). Accordingly, both the percentages and cell numbers of *Phf23*$^{-/-}$ B220$^+$ cells in BM and spleen were significantly less than those of WT (Supplementary Fig. S4D–F). Thus, *Phf23* deficiency impaired B-cell differentiation, which may contribute to the development of B malignancies.

Identifying a PHF23–SIN3–HDAC Complex Mediated by the N-Terminus of PHF23

To further understand how PHF23 regulated gene expression, we performed a co-immunoprecipitation mass spectrometry (Co-IP/MS) assay to identify potential PHF23 binding partners. Interestingly, the top hits were SIN3 transcription regulator family members A and B (SIN3A and SIN3B; Supplementary Table S2). SIN3 is a master scaffold protein in the SIN3–HDAC corepressor complex, which represses transcription and is involved in various biological and cellular processes (34, 35). The SIN3–HDAC (histone deacetylase) complex contains multiple tightly associated components, and notably all of them were co-immunoprecipitated with PHF23 in our Co-IP/MS assay, including HDAC1 and HDAC2, the core catalytic proteins of this complex, and 9 other factors: SAP130, FAM60A, RBBP7, RBBP4, ARID4B, SUDS3, SAP30L, BRMS1L, and SAP30 (Fig. 4A and Supplementary Table S2; refs. 36, 37). The interactions of PHF23 with SIN3A and HDAC1 were confirmed with Co-IP followed by Western blotting (Fig. 4B). The endogenous PHF23–SIN3–HDAC (PSH) complex was further validated by Co-IP with an antibody against PHF23 (Fig. 4C). We noticed that ING2, another H3K4me3 reader that has been reported to bind the SIN3–HDAC complex and associated with gene repression (38, 39), was not detected by PHF23 Co-IP/MS. These results suggested that PHF23 directly interacted with the SIN3–HDAC complex to form a PSH complex.

PHF23 contains multiple functional domains, including the PHD zinc finger domain at the C-terminus that can bind H3K4me3 in a sequence-specific manner and a coiled-coil domain in the middle that might mediate protein–protein interactions, whereas the N-terminus has been less characterized (ref. 20; Supplementary Fig. S5A). We tested which region of PHF23 interacted with the SIN3–HDAC complex with PHF23-truncated mutants. Interestingly, we found that neither coiled-coil nor PHD domain truncations (ΔCC and ΔPHD) affected the binding of PHF23 with SIN3A and HDAC1. However, the N-terminus truncation (ΔN) completely disrupted the interactions between PHF23 and SIN3A–HDAC1 (Fig. 4D). Thus, the N-terminus of PHF23 was essential for the PSH complex.

The PSH Complex Coordinates H3K4me3 and H3K27ac for Gene Activation

Histone deacetylation is one of the gene-regulation mechanisms, and here we focused on the deacetylation of H3K27ac, an active histone marker (30, 40, 41). To test the effect of the PSH complex on H3K27ac, we measured the total H3K27ac levels of *Phf23*-deficient cells by Western blotting. As shown in Fig. 4E, H3K27ac was significantly reduced in *Phf23*$^{+/-}$ FLCs compared with that in *Phf23*$^{+/+}$ FLCs. To further understand the regulation of PHF23 on the functions of the SIN3–HDAC complex, we analyzed ChIP-seq data with HDAC1 or H3K27ac antibody (Supplementary Fig. S5B and C). Consistent with the interaction between PHF23 and the SIN3–HDAC complex, PHF23 binding sites significantly overlapped with HDAC1 binding peaks at both transcription start sites (TSS) and enhancer regions (Fig. 4F). Importantly, the binding of PHF23 significantly increased the H3K27ac levels compared with those with only HDAC1 binding at both TSSs and

Figure 4. PHF23 directly binds and negatively regulates the SIN3–HDAC complex. **A,** Schematic diagram of the PSH complex. Colors indicate the Mascot scores of each component measured by Co-IP of FLAG–PHF23 and LC/MS. **B,** Representative Western blotting pictures showing FLAG–PHF23, SIN3A, and HDAC1 of input and FLAG–PHF23 Co-IP. **C,** Representative Western blotting pictures of endogenous PHF23, SIN3A, and HDAC1 of input and Co-IP with IgG or PHF23 antibodies. **D,** Representative Western blotting pictures of FLAG–PHF23, SIN3A, and HDAC1 of input and FLAG-tagged full-length or truncated PHF23 Co-IP. **E,** Representative Western blotting pictures of PHF23 and H3K27ac in *Phf23*$^{+/+}$ and *Phf23*$^{+/-}$ FLCs. **F,** Venn diagrams showing overlapping of PHF23 and HDAC1 bound genes, analyzed by ChIP-seq. *P*, Fisher exact test. Left, HDAC1 bound at TSS; right, HDAC1 bound at enhancer regions. **G,** Mean $\log_2$ H3K27ac levels on genes with no binding (without HDAC1 TSS and PHF23 binding), HDAC1_T (only HDAC1 at TSS), PHF23 only, or cobinding (both HDAC1 and PHF23 binding at TSS) in Ba/F3 cells. P_{adj}, Wilcoxon signed-rank test. **H,** Mean $\log_2$ H3K27ac levels on genes with no binding (without HDAC1 enhancer and PHF23 binding), HDAC1_E (only HDAC1 at enhancer regions), PHF23 only, or cobinding (both HDAC1_E and PHF23 binding). P_{adj}, Wilcoxon signed-rank test. **I,** Mean of $\log_2$ TPM of genes with no binding (without HDAC1 TSS and PHF23 binding), HDAC1_T (only HDAC1 at TSS), PHF23 only, or cobinding (both HDAC1 and PHF23 binding at TSS) in immature B-lymphoblastic malignancy cells. P_{adj}, Wilcoxon signed-rank test. **J,** Mean of $\log_2$ TPM of genes with no binding (without HDAC1 enhancer and PHF23 binding), HDAC1_E (only HDAC1 at enhancer regions), PHF23 only, or cobinding (both HDAC1_E and PHF23 binding). **K,** GSEA showing the negative enrichment of the SENESE_HDAC1_TARGETS_UP gene set in sh*Phf23* pre-B cells compared with sh*Ren* cells (NES = −1.33; FDR $q = 0.00$). **L,** Top five KEGG pathways enriched in genes cobound by both PHF23 and HDAC1. **M,** Venn diagram showing overlapping of the PHF23 bound genes and the p53 pathway genes. *P*, Fisher exact test. **N,** Percentages of genes with H3K4me3 binding in p53 pathway genes with PHF23 binding or p53 pathway genes without PHF23 binding. **O,** Percentages of genes with H3K27ac binding in p53 pathway genes with PHF23 binding or p53 pathway genes without PHF23 binding. **P,** IGV plots showing PHF23, HDAC1, H3K27ac, and H3K4me3 binding density on *Cdkn1a*.

Downloaded from cancerdiscovery.aacrjournals.org on December 30, 2020. © 2020 American Association for Cancer Research.

Published OnlineFirst September 25, 2020; DOI: 10.1158/2159-8290.CD-20-0336

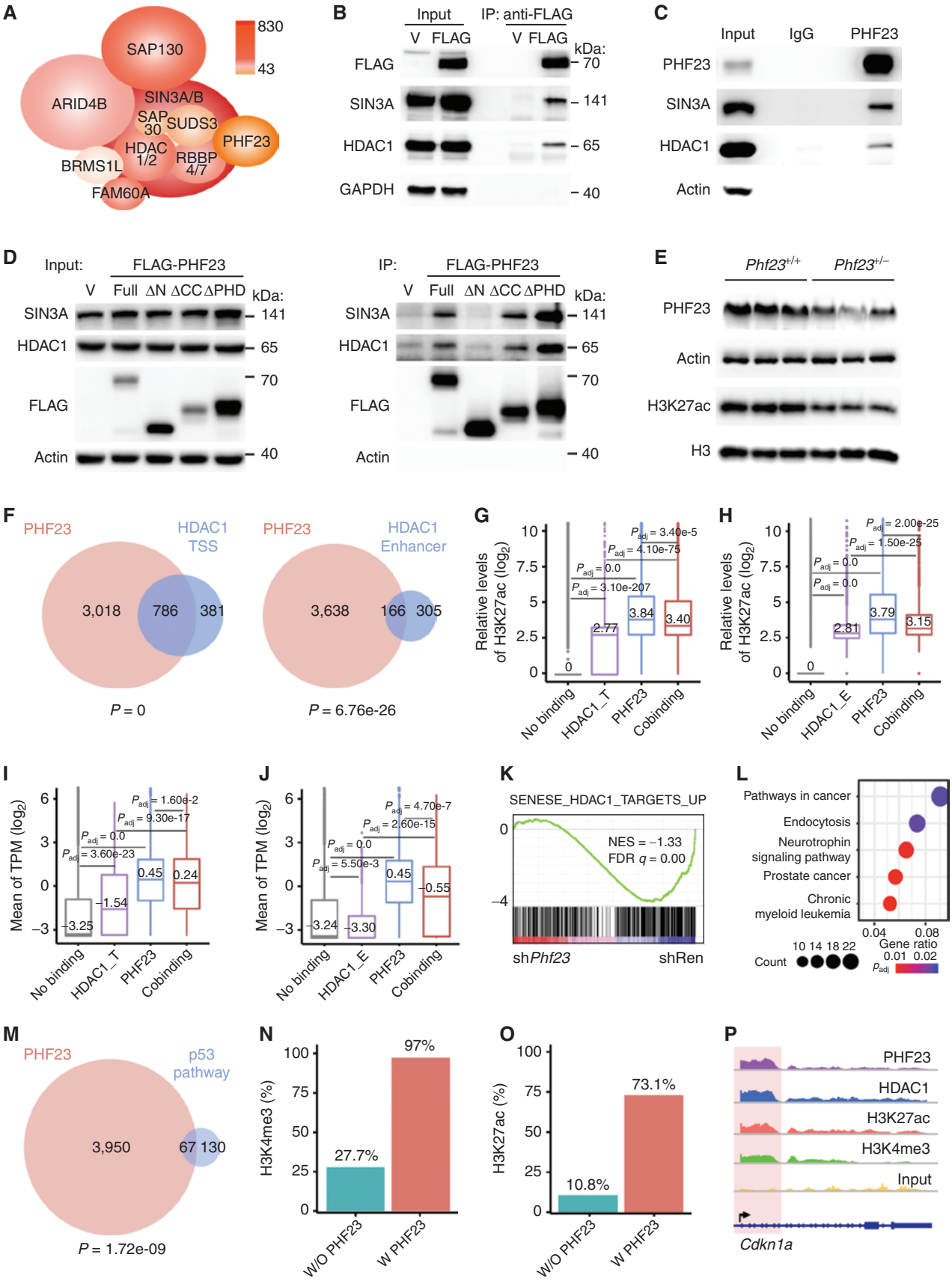

Downloaded from cancerdiscovery.aacrjournals.org on December 30, 2020. © 2020 American Association for Cancer Research.

Published OnlineFirst September 25, 2020; DOI: 10.1158/2159-8290.CD-20-0336

enhancer regions (Fig. 4G and H). Of TSSs with both HDAC1 and PHF23, 79.8% were associated with H3K27ac, whereas only 31.3% of HDAC1-bound TSSs were associated with H3K27ac. Similar correlations were observed in the enhancer regions (Supplementary Fig. S5D). These results suggested that PHF23 repressed the deacetylation activity of HDAC1 on H3K27ac.

Increased H3K27ac levels are associated with the upregulation of target genes (30, 41). To analyze the effect of the PSH complex on gene regulation, we analyzed RNA-seq data of sh*Phf23* tumor cells compared with those with WT *Phf23*. The expression levels of genes associated with both PHF23 and HDAC1 were significantly higher than those with only HDAC1 in lymphomas/leukemias (Fig. 4I and J). A similar expression pattern was also observed in pre–B cells (Supplementary Fig. S5E and F). H3K27ac binding sites were largely overlapped with those of H3K4me3, and both were associated with higher gene-expression levels of targets compared with those without these histone markers (Supplementary Fig. S5G and H). Even among the genes with both H3K4me3 and H3K27ac, those with PHF23 binding had significantly higher expression levels than those without PHF23 binding (Supplementary Fig. S5I and J). In particular, GSEA showed that the SENESE_HDAC1_TARGETS_UP gene set was significantly downregulated in sh*Phf23* pre–B cells (NES = –1.33, FDR $q = 0.00$), which was consistent with the interaction of PHF23 and the SIN3–HDAC complex (Fig. 4K). Thus, the PSH complex might be a critical regulator of gene expression in both premalignant and malignant cells.

The most enriched Kyoto Encyclopedia of Genes and Genomes (KEGG) pathways in PHF23 and HDAC1 cobound genes were pathways in cancer and leukemia (Fig. 4L). Because *PHF23* was codeleted with *TP53* in human cancers with 17p deletions (3, 8) and loss of both synergistically promoted tumorigenesis (Fig. 2H–J), we wondered if the PSH complex would directly regulate the p53 pathway. We found that 67 of the 197 p53 target genes ($P = 1.72e-09$) were bound by PHF23 (ref. 42; Fig. 4M). Consistent with the potential function of the PSH complex to link the two active histone markers H3K4me3 and H3K27ac, most of the PHF23 bound p53 target genes were also associated with H3K4me3 and H3K27ac (Fig. 4N and O and Supplementary Fig. S5K and L). As a result, the p53 pathway was significantly negatively enriched in sh*Phf23* lymphoma/leukemia cells compared with those with sh*Ren* (Fig. 2J). Among these PSH target genes were multiple well-known p53 targets, including *Cdkn1a, Bax*, and *Mdm2*. These genes were cobound by PHF23 and HDAC1 and also associated with histone markers H3K4me3 and H3K27ac in Ba/F3 cells (Fig. 4P and Supplementary Fig. S5M and N). Taken together, these biochemical and multiomics data suggested that the PSH complex might link the two active histone markers, H3K4me3 and H3K27ac, for synergistically regulating gene activation, including of p53 pathway genes.

The PSH Complex Is Critical for Tumorigenesis and Maintenance

Given the importance of the PSH complex in histone modifications and gene regulation, we wondered whether this complex plays significant roles in lymphoma/leukemia genesis and maintenance. SIN3A and its associated HDAC1 and HDAC2 have been shown to be required for normal hematopoiesis (43). We found that knockdown of *Sin3a* completely blocked the development of *Phf23*$^{+/-}$*;Myc* lymphoma/leukemia (Fig. 5A and B). Similarly, *Sin3b* deficiency also significantly extended the tumor-free survival of mice transplanted with *Ph23*$^{+/-}$*;Myc* FLCs (Fig. 5C and D). The latencies of *Ph23*$^{+/-}$*;Myc* lymphoma/leukemia were correlated with the knockdown efficiencies of sh*Sin3b*. These *in vivo* functional studies suggested that the SIN3–HDAC complex is essential for lymphomagenesis driven by *Phf23* loss.

Furthermore, we tested the potential roles of the PSH complex in tumor maintenance. We reduced the expression of *Sin3a* by shRNA in sh*Phf23* lymphoma/leukemia cells as well as Ba/F3 cells, which worked as a control to rule out general cytotoxicity of *Sin3a* deficiency. The results showed that *Sin3a* knockdown specifically impaired lymphoma/leukemia cell growth with *Phf23* loss but had a mild effect on Ba/F3 cells (Fig. 5E and Supplementary Fig. S6A). *Sin3b* suppression had a similar effect on sh*Phf23* lymphoma/leukemia cells as *Sin3a* deficiency but had little effect on untransformed Ba/F3 cells (Fig. 5F and Supplementary Fig. S6B). Furthermore, *Hdac1* shRNAs significantly reduced the survival of *Phf23*-deficient lymphoma/leukemia compared with sh*Ren* (Fig. 5G). The HDAC inhibitors entinostat, mocetinostat, and chidamide specifically induced the death of sh*Phf23* lymphoma/leukemia cells but not control Ba/F3 cells at the given concentrations, suggesting a potential therapeutic window of these small molecules for *Phf23*-deficient cancers (Fig. 5H).

To explore the molecular effects of HDAC inhibitors on *Phf23*-deficient tumor cells, we performed RNA-seq analyses of sh*Phf23* lymphoma/leukemia cells treated with or without entinostat or chidamide. Interestingly, the upregulated genes in HDAC inhibitor–treated cells significantly outnumbered the downregulated genes, opposite to what was observed in sh*Phf23* cells (35 and 176 genes upregulated and downregulated, respectively, by sh*Phf23* versus 384 and 33 genes upregulated and downregulated, respectively, by HDAC inhibitors; $\log_2$ fold change >1 or <–1, $P_{adj} < 0.05$; Supplementary Fig. S6C and D and Supplementary Tables S3–4). GSEA showed that the upregulated genes in sh*Phf23* cells were significantly negatively enriched in lymphoma/leukemia cells treated with either chidamide or entinostat (chidamide: NES = –1.49, FDR $q = 0.00$; entinostat: NES = –1.34, FDR $q = 0.04$), whereas the downregulated genes in sh*Phf23* cells were significantly positively enriched (chidamide: NES = 2.05, FDR $q = 0.00$; entinostat: NES = 1.89, FDR $q = 0.00$; Fig. 5I and J and Supplementary Fig. S6E). Thus, treatment with HDAC inhibitors reversed the effects of *Phf23* loss on gene regulation.

Because the N-terminus of PHF23 was the key domain mediating the formation of the PSH complex, we introduced full-length or other PHF23 mutants into *Phf23*-deficient tumor cells. Here, we used *Phf23*$^{+/-}$ lymphoma/leukemia cells instead of sh*Phf23* cells to avoid the interference between shRNAs and exogenous cDNAs. Full-length PHF23 specifically repressed *Phf23*$^{+/-}$ lymphoma/leukemia but did not exhibit a significant effect on Ba/F3 cells, which further confirmed *Phf23* as a bona fide TSG (Fig. 5K and Supplementary S6F). In contrast, ΔN PHF23 completely lost its tumor-suppression function, which strongly suggested that dysfunction of the PSH complex, mediated by the N-terminus of PHF23, was required for tumor maintenance. ΔPHD PHF23 had a significantly reduced repression effect on *Phf23*$^{+/-}$ lymphoma/

Downloaded from cancerdiscovery.aacrjournals.org on December 30, 2020. © 2020 American Association for Cancer Research.

Published OnlineFirst September 25, 2020; DOI: 10.1158/2159-8290.CD-20-0336

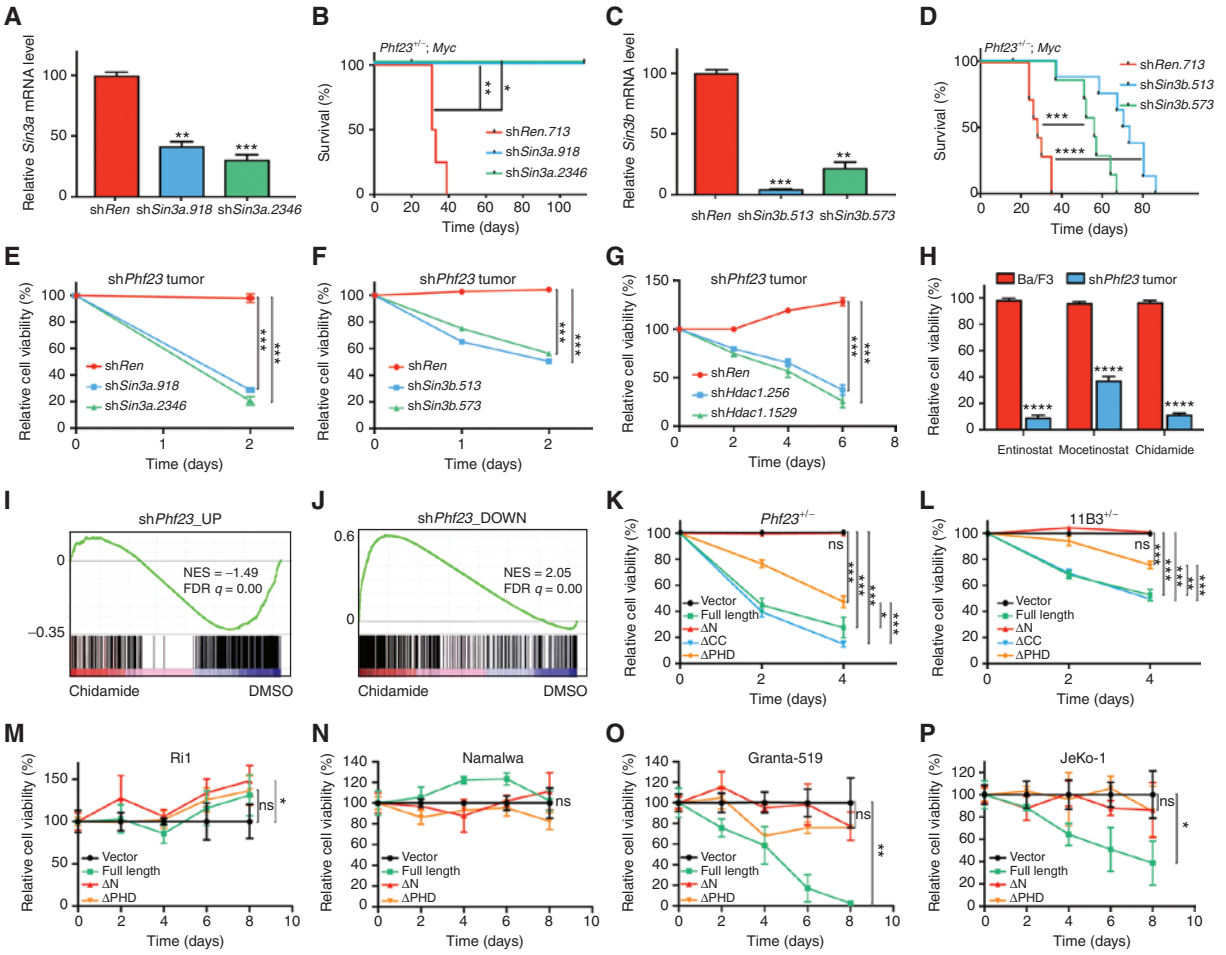

Figure 5. The PSH complex dysregulation was critical for tumorigenesis and maintenance. **A,** Knockdown efficiencies of sh*Sin3a*, measured by qPCR. **B,** Kaplan–Meier tumor-free survival curves of recipient mice transplanted with *Phf23*$^{+/-}$ FLCs with *Myc*-linked sh*Sin3a* or sh*Ren*. $n = 4$. *, $P < 0.05$; **, $P < 0.01$ (log-rank test). **C,** Knockdown efficiencies of sh*Sin3b* measured by qPCR. **D,** Kaplan–Meier tumor-free survival curves of recipient mice transplanted with *Phf23*$^{+/-}$ FLCs infected with *Myc*-linked sh*Sin3b* or sh*Ren*. $n = 8$. ***, $P < 0.001$; ****, $p < 0.0001$ (log-rank test). **E,** Relative cell viabilities of sh*Phf23* lymphoma/leukemia cells with sh*Sin3a*. $n = 3$. **F,** Relative cell viabilities of sh*Phf23* lymphoma/leukemia cells with sh*Sin3b*. $n = 3$. **G,** Relative cell viabilities of sh*Phf23* lymphoma/leukemia cells with sh*Hdac1*. $n = 3$. **H,** Relative cell viabilities of Ba/F3 cells and sh*Phf23* lymphoma/leukemia cells treated with HDAC inhibitors (entinostat, 0.5 μmol/L; mocetinostat, 0.1 μmol/L; chidamide, 0.5 μmol/L). $n = 3$. **I,** GSEA showing the negative enrichment of the sh*Phf23* upregulated gene set in chidamide-treated sh*Phf23* lymphoma/leukemia cells compared with DMSO-treated cells (NES = −1.49; FDR $q = 0.00$). **J,** GSEA showing the positive enrichment of the sh*Phf23* downregulated gene set in chidamide-treated sh*Phf23* lymphoma/leukemia cells compared with DMSO-treated cells (NES = 2.05; FDR $q = 0.00$). **K,** Relative cell viabilities of *Phf23*$^{+/-}$;*Myc* lymphoma/leukemia cells transduced with full-length or truncated *Phf23*. $n = 3$. **L,** Relative cell viabilities of chromosome 11B3-deleted lymphoma/leukemia cells transduced with full-length or truncated *Phf23*. $n = 3$. **M,** Relative cell viabilities of 17p intact Ri1 human lymphoma cells transduced with full-length or truncated *PHF23*. $n = 3$. **N,** Relative cell viabilities of 17p intact Namalwa human lymphoma cells transduced with full-length or truncated *PHF23*. $n = 3$. **O,** Relative cell viabilities of 17p-deleted Granta519 human lymphoma cells transduced with full-length or truncated *PHF23*. $n = 3$. **P,** Relative cell viabilities of 17p-deleted JeKo1 human lymphoma cells transduced with full-length or truncated *PHF23*. $n = 3$. **A, C, E–H,** and **K–P,** *, $P < 0.05$; **, $P < 0.01$; ***, $P < 0.001$; ns, not significant (unpaired two-tailed *t* test).

leukemia, indicating that the H3K4me3 binding activity was required for the tumor suppression function of PHF23, whereas ΔCC had a minimal effect (Fig. 5K). Taken together, these results indicated that deficiency of the PSH complex was critical for the maintenance of tumors with *Phf23* loss.

Given the large number of genes located on chromosome 17p and the seemingly dominant effect of *TP53*, we wondered if the PSH complex played significant roles in del(17p) cancers. We transduced full-length, ΔN, ΔCC, and ΔPHD PHF23 into mouse immature B-lymphoblastic malignancy cells with deletion of chromosome 11B3, which highly resembled human cancers with 17p deletions (8). PHF23 restoration significantly reduced the survival of chromosome 11B3–deleted tumor cells, emphasizing that PHF23 significantly contributed to the pathology of chromosome 17p–deleted cancers (Fig. 5L). Furthermore, ΔPHD PHF23 had impaired tumor suppression function on chromosome 11B3–deleted lymphoma/leukemia, suggesting the importance of the PSH complex for the function of chromosome 17p. To further validate the functions of the PSH complex in human cancers, we transduced WT or mutant PHF23 into human lymphoma cells with or without 17p deletions. We found that WT PHF23 significantly inhibited the growth of 17p-deleted Granta519 and JeKo1 cells, whereas it had no

Downloaded from cancerdiscovery.aacrjournals.org on December 30, 2020. © 2020 American Association for Cancer Research.

Published OnlineFirst September 25, 2020; DOI: 10.1158/2159-8290.CD-20-0336

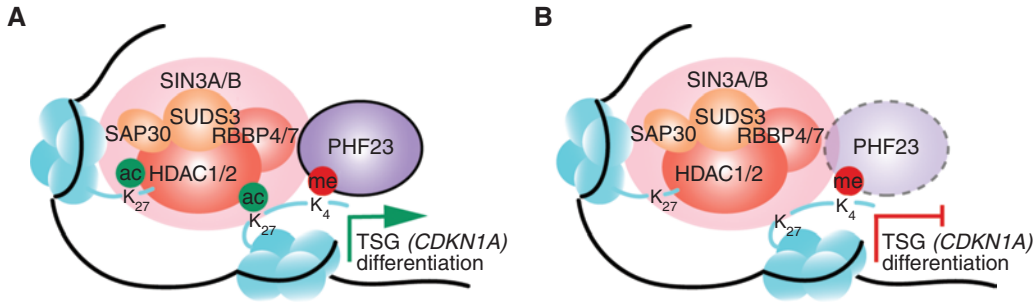

Figure 6. Schematic diagram showing the working model for the PSH complex in normal and tumor cells. **A,** Schematic diagram showing the working model of the PSH complex in B-cell differentiation and TSG regulation. **B,** Schematic diagram showing the working model of the PSH complex in tumor cells with *PHF23* deficiency.

effect on 17p-intact Ri1 and Namalwa cells (Fig. 5M–P). Furthermore, consistent with our findings in murine lymphoma/leukemia cells, ΔN PHF23 completely lost its tumor-suppression activity. These data strongly suggested that *PHF23* deficiency significantly contributed to the pathology of del(17p) cancers, which gave rise to an unexpected susceptibility for treatments targeting the dysregulated PSH complex.

Taken together, our data identified *PHF23* as a 17p TSG, loss of which was critical for both tumorigenesis and tumor maintenance and significantly contributed to the pathology of 17p-deleted cancers. PHF23 colocalized with the active histone marker H3K4me3 and directly bound and repressed the SIN3–HDAC complex through its N-terminus. The PSH complex provides a synergistic link between H3K4me3 and H3K27ac for gene activation, especially TSGs and differentiation genes (Fig. 6A and B).

DISCUSSION

Given the prevalence of CNVs in human cancers and their association with poor prognosis, it is important to understand the underlying mechanisms of CNVs in tumorigenesis and treatment. In this study, we identify *PHF23* on chromosome 17p13.1 as a haploinsufficient TSG with multiple *in vivo* functional genetic strategies. Remarkably, *PHF23* deficiency always happens together with chromosome 17p loss, and although there are very few independent mutations in human cancers, we wonder whether *PHF23* loss contributes to tumorigenesis in the context of loss of other co-occurring 17p genes, especially *TP53*. We demonstrate that *PHF23* can cooperate with *TP53*, which is generally codeleted with *PHF23* in human cancers, through corepressing the expression of their common downstream target genes. We propose that, whereas haploinsufficiencies of either *PHF23* or *TP53* would have mild effects on the p53 pathway, the cooperation of both on the same pathway may have synergistic effects to give rise to significant repression of this pathway and thus promote tumorigenesis. This model would help to explain the significance of 17p deletions and potentially other CNVs with multiple TSGs, as a whole, during tumorigenesis. Altogether, our studies on *PHF23* provide an example for identifying other potential TSGs and exploring their mechanisms involved in CNVs in human cancers.

PHF23 has been proposed to be an H3K4me3 reader (20), and our study demonstrates that PHF23 can form a PSH complex together with the SIN3–HDAC complex, an eraser of H3K27ac. PHF23 directly binds with the SIN3–HDAC complex through its N-terminus and restrains its deacetylation capacity on H3K27ac. Hence, the PSH complex provides a direct link between the two active histone markers for their synergistic regulation of gene activation. The PSH complex is distinguishable from the ING2–SIN3–HDAC complex (38, 39). ING2, also a PHD finger protein and H3K4me3 reader, directly binds and enhances the deacetylation activity of the SIN3–HDAC complex, which leads to gene repression (38). It would be interesting to dissect the potential competitions between the PSH complex and the ING2–SIN3–HDAC complex for H3K4me3 sites for gene regulation and their paradoxical potential cooperation for biological processes, including tumorigenesis.

It is intriguing that, in contrast to the haploinsufficient loss of *PHF23* in human cancers with 17p deletions, *PHF23* is also involved in AML through chromosome translocation to form an oncofusion protein, NUP98–PHF23 (8, 18, 19). NUP98–PHF23 binds to specific H3K4me3 sites and drives an AML program with upregulated HOX genes. Paradoxically, *PHF23* loss in del(17p) cancers seems to have dysregulation of the SIN3–HDAC complex and results in decreased expression of B-cell differentiation genes and other TSGs. Therefore, distinct mechanisms underlie different *PHF23* genetic alterations in AML and lymphoma. We believe that the reason might be the N-terminus of PHF23, which is critical for the formation of the PSH complex and the tumor suppression function of PHF23. The N-terminus of PHF23 is deleted in AML-associated NUP98–PHF23 (18, 19), which can also at least partially contribute to the pathology of human AML. Interestingly, the translocation of *NUP98–PHF23* results in not only an oncogenic fusion protein (NUP98–PHF23) but also loss of one copy of *NUP98* and *PHF23*. It is very interesting to test whether the disruption of one allele of *PHF23* in NUP98–PHF23 AML would contribute to the disease. Our studies, together with others, illustrate the complexity of the molecular mechanisms underlying genetic abnormalities in human cancers.

Importantly, we show that, although only one of the several hundred genes involved in del(17p), *PHF23* haploinsufficiency is required for the maintenance of human cancers with 17p deletions, which suggests an unexpected susceptibility for these refractory diseases. Future work testing HDAC inhibitors and other potential drugs related to the PSH complex may be beneficial for patients in clinical practice.

Downloaded from cancerdiscovery.aacrjournals.org on December 30, 2020. © 2020 American Association for Cancer Research.

Published OnlineFirst September 25, 2020; DOI: 10.1158/2159-8290.CD-20-0336

METHODS

Mice

All mouse experiments were approved by the Institutional Animal Care and Use Committees of Sichuan University. *Eμ–Myc* mice were from Jackson Laboratories (22). Pre–B cells were enriched from 6- to 8-week-old C57BL/6 (cat. 219; Charles River) BM by autoMACS purification with Biotin anti-mouse/human CD45R/B220 (cat. 103204, RRID:AB_312989; BioLegend) and anti-Biotin microbeads (cat. 130–090–485, RRID:AB_244365; Miltenyi Biotec). Purified pre–B cells were cultured in RPMI 1640 medium supplemented with 20% FBS and 10 ng/mL IL7 (cat. 407-ML-200; R&D). For *in vivo* tumorigenesis, pre–B cells or E13.5 FLCs were transduced with retroviruses carrying shRNA or CRISPR/Cas9, respectively, and injected intravenously into sublethally irradiated (4.5 Gy) C57BL/6 recipient mice (6–8 weeks old, male). All recipient mice were randomly divided into each group before transplantation and monitored twice per week by palpation. The tumor monitoring process was done as blinded experiments. The immunophenotypes of resulting lymphomas were analyzed by flow cytometry using antibodies purchased from BioLegend. Statistical analysis of all survival data was accomplished with the log-rank test from Prism 8.

Phf23 knockout mice were generated in the Genetically Engineered Mouse Facility of State Key Laboratory of Biotherapy with CRISPR/Cas-mediated gene-editing technology as described before (44). Briefly, *Phf23* sgRNA (targeting sequence: ATCATGGGCCGCC CCGCAA) and Cas9 mRNA were delivered into C57BL/6 zygotes by microinjection, followed by transplantation into the uterus of surrogate CD-1(ICR) female mice. A 14-bp insertion leading to a premature stop codon occurred at the sgRNA targeted sites. The resulting *Phf23* knockout mouse was back-crossed to WT C57BL/6 mouse for more than eight generations to get rid of potential off-target mutations.

BM Transplantation

The BM cells from femurs and tibia of CD45.1 donor mice and E14.5 FLCs harvested from CD45.2 *Phf23* knockout mice were mixed and transplanted into lethally irradiated CD45.1 C57BL/6 recipient mice. Four months after transplantation, recipient mice were sacrificed for analyses.

Retroviral Constructs

MirE-based shRNAs were cloned into retroviral constructs, including MSCV–shRNA–SV40–*Myc*–IRES–GFP, MSCV–shRNA–IRES–mCherry, and MSCV–shRNA–PGK–Puro–IRES–GFP, as previously reported (8, 13, 25). The sequences of shRNAs targeting *Renilla* or *Trp53* are from published reports (8, 13, 25), and the sequences of shRNAs targeting *Phf23, Sin3a, Sin3b*, and *Hdac1* are listed in Supplementary Table S5. sg*Phf23*: ATCATGGGCCGCCCCGCAA. Retrovirus packaging and infection were done as previously reported (8, 13, 25).

Cell Line Culture

Ba/F3 (#HB-283), HeLa (#CCL-2), 293T (#CRL-1573), JeKo1 (#CRL-3006), and Namalwa (#CRL-1432) were from ATCC, and Granta519 (#ACC342) and Ri1 (#ACC585) were from DSMZ. The 17p status of JeKo1, Granta519, Ri1, and Namalwa has been confirmed by qPCR. All human lymphoma cell lines were cultured at 37°C with 5% CO_2 in RPMI 1640 medium supplemented with 10% v/v FBS and penicillin (100 U/mL)/streptomycin (0.1 mg/mL). Ba/F3 cells were maintained in RPMI 1640 medium supplemented with 10% v/v FBS and 2 ng/mL IL3 (cat. 403-ML-050; R&D). All cell lines were routinely tested for *Mycoplasma* by PCR. Experiments were performed within 4 weeks after fresh viable cells were thawed.

Co-IP and Immunoblotting

The 3xFLAG-tagged full-length, ΔN (2–119 aa deleted), Δcoiled-coil (225–283 aa deleted), and ΔPHD domain (331–393 aa deleted) *Phf23* cDNA were cloned into retroviral construct MSCV–IRES–mCherry and transduced into Ba/F3 cells. mCherry$^+$ cells were sorted out by FACS (Aria III; BD Biosciences). Then, the whole-cell lysates were extracted with cell lysis buffer (Cell Signaling Technology) supplemented with protease inhibitor cocktail (Roche) and incubated with anti-FLAG M2 mAb-conjugated agarose beads (cat. A2220, RRID:AB_10063035; Sigma-Aldrich). For endogenous PHF23 Co-IP, 10^7 HeLa cells were lysed and incubated with IgG or PHF23 antibody. The horseradish peroxidase (HRP)–conjugated FLAG antibody was purchased from Sigma-Aldrich (cat. A8592, RRID:AB_439702); the anti-SIN3A antibody was from Thermo Fisher Scientific (cat. PA1–870, RRID:AB_2187625); the anti-HDAC1 antibody was from Cell Signaling Technology (cat. 34589, RRID:AB_2756821); the anti-PHF23 antibody, recognizing its C-terminus, was from Bethyl (cat. A302–320A, RRID:AB_1850230) for Co-IP and Western blotting; the anti-IgG antibody was from Abcam (cat. ab171870, RRID:AB_2687657); the anti-GAPDH antibody was from BioXcell (BX-008); and HRP-conjugated actin antibody was from Thermo Fisher Scientific (cat. MA5–32540, RRID:AB_2809817).

Liquid Chromatography–Mass Spectrometry

The preparation of samples for mass spectrometric analysis was conducted according to procedures reported previously (45). In brief, the immunoprecipitated protein products were prepared as described above and eluted with 0.1% trifluoroacetic acid. After being condensed and dried in the speed vacuum, the lyophilized protein mixtures were digested into peptides using sequence-grade trypsin resolved in triethylammonium bicarbonate. The tryptic peptides were further reduced by 10 mmol/L dithiothreitol at 56°C for 1 hour, alkylated with 55 mmol/L iodoacetamide in the dark at room temperature for an additional 45 minutes, and again dried in the speed vacuum. The lyophilized peptides were desalted with C18 ZipTip (Millipore). First, the ZipTips were equilibrated successively with 100% acetonitrile (ACN), 50% ACN/ddH_2O, and 0.1% fluoroacetic acid (FA). The peptides resolved in approximately 20 μL 0.1% FA were then loaded onto ZipTips and washed extensively with 0.1% FA and eventually eluted with 50% ACN/ddH_2O. The eluates were analyzed by a Q-Exactive Plus instrument available at the State Key Laboratory of Biotherapy.

Quantitative PCR

All primers used for qPCR analysis are listed in Supplementary Table S6. To detect the knockdown efficiencies of shRNAs targeting *Phf23*/*Sin3a*/*Sin3b*/*Hdac1*, Ba/F3 cells were infected with MSCV–mirE–PGK–Puro–IRES–GFP retroviruses, followed by 1 μg/mL puromycin (Gibco). For detection of *Phf23* expression level in eventual malignant cells, tumor cells were isolated from lymph nodes of diseased mice upon sacrifice. sh*Trp53;Myc* lymphoma/leukemia cells were used as control. For qPCR, RNA was isolated with TRIzol, cDNA was synthesized with M-MLV (Invitrogen), SYBR Green PCR Master Mix (Applied Biosystems) was used, and qPCR was performed on a Quantstudio3 (Applied Biosystems).

In vitro *Drug Response Assays*

Lymphoma/leukemia cell lines generated from *Phf23* knockdown or 11B3 deletion tumor-bearing mice were cultured in BCM medium [45% DMEM, 45% Iscove's modified Dulbecco's medium, 10% FBS, 2 mmol/L glutamine, 50 μM β-mercaptoethanol, penicillin (100 U/mL)/streptomycin (0.1 mg/mL)] and were plated in 96-well plates with a cell density of 10,000 cells per well. The plated cells were treated with the indicated concentrations of HDAC inhibitors (Selleck) or DMSO. The number of living cells was counted by BD Accuri C6.

Rescue Assay

Tumor cells were infected with the indicated retroviruses, and the percentages of mCherry$^+$ populations were measured every other day with LSRFortessa flow cytometry. The cell numbers were counted by

Downloaded from cancerdiscovery.aacrjournals.org on December 30, 2020. © 2020 American Association for Cancer Research.

Published OnlineFirst September 25, 2020; DOI: 10.1158/2159-8290.CD-20-0336

BD Accuri C6 every other day. The relative cell viability of mCherry$^+$ or GFP$^+$ cells was calculated by dividing by the percentages of those with empty vectors.

RNA-seq Analysis

Pre–B cells isolated from mouse BM were first infected with eMLM–sh*Ren* or eMLM–sh*Phf23*, respectively, and 48 hours after infection, the GFP-positive cells were sorted out by FACS Aria III for RNA-seq. *Phf23* knocked-down or control sh*Ren* lymphoma/leukemia cells were harvested from enlarged lymph nodes of recipient mice for RNA-seq. sh*Phf23* lymphoma/leukemia cells treated with HDAC inhibitors, chidamide (0.5 μmol/L), entinostat (0.5 μmol/L), or DMSO as a control for 12 hours were harvested for RNA-seq. RNA-seq libraries were prepared by the NEBNext Ultra RNA Library Prep Kit for Illumina, lymphoma/leukemia cells' RNA-seq and HDAC inhibitor–treated cells' RNA-seq were sequenced by the Illumina NovaSeq 6000 sequencing machine with 150-bp paired-end reads, and pre–B RNA-seq were sequenced by a BGISEQ500 sequencing machine (Beijing Genomic Institute, Shenzhen, China) with 50-bp single-end reads. The RNA-seq reads were aligned to the reference genome (GRCm38) by STAR_2.6.0a. Transcript abundance was normalized and measured by TPM. Differential gene expression was analyzed by DESeq2 (RRID:SCR_000154). Genes with an absolute fold change greater than 1 and $P_{adj} \leq 0.05$ were counted as differentially expressed genes. The heat maps of differentially expressed genes were done by pheatmap (RRID:SCR_016418) and normalized by *z* score. The TPM data were used for GSEA. To identify functional categories of differentially expressed genes, Gene Oncology enrichment analysis was performed using the R package clusterProfiler (RRID:SCR_016884).

ChIP-seq

ChIP assays were performed according to a modified Micrococcal nuclease (MNase)–based ChIP-seq protocol reported previously (46). Briefly, 10 million Ba/F3 cells stably expressing FLAG-tagged *Phf23* were harvested, resuspended in PBS, and cross-linked in 4% formaldehyde solution. Nuclei were washed, then digested using MNase (cat. M0247S, 2000 gel units/μL; NEB), and the samples were sonicated in the Diagenode Bioruptor (30 seconds on, 30 seconds off for 15 cycles). Incubation with the indicated antibodies was performed overnight at 4°C. FLAG M2 mAb-conjugated agarose beads and HDAC1 antibody were mentioned above, and H3K4me3 (cat. ab8580, RRID:AB_306649) and H3K27ac (cat. ab4729, RRID:AB_2118291) antibodies were from Abcam. DNA was eluted with 100 μL ChIP elution buffer, followed by purification with the Qiagen MinElute PCR Purification Kit, and sequenced by Novogene. Adaptor sequences were trimmed for all paired-end reads and mapped against the mm10 reference genome with STAR_2.6.0a. Bam files were transformed to bigwig files by Deeptools (RRID:SCR_016366) (47) and normalized by Bins Per Million (BPM) mapped reads. Integrative Genomics Viewer visualization was used for peak visualization. The heat map and Average Profile of chip peaks were performed by Deeptools. Peaks were called by macs2 2.1.1 with a *q* value <0.01. The DiffBind (RRID:SCR_012918) was used to annotate the peaks, and only the genes binding in both biological repeats were counted. Venn diagrams were generated with the R package of VennDiagram (RRID:SCR_002414). The overlapping genes were used as an input list to calculate enrichment score in all gene sets of KEGG (RRID:SCR_012773) pathways via clusterProfiler.

Statistical Analysis

Statistical test methods, sample sizes, and *P* values are indicated in the corresponding figure legends. Statistical analyses were performed using GraphPad Prism (RRID:SCR_002798; GraphPad Software). The log-rank test was used to compare survival differences among groups for Kaplan–Meier tumor-free survival curve. Data were tested for statistical significance by an unpaired two-tailed *t* test, except the data in Figure 3H–K and Supplementary Fig. S4E and F, which were tested by an unpaired one-tailed *t* test. The relative protein gray scale was analyzed by ImageJ (RRID:SCR_003070; National Institutes of Health). *P* values for the Venn diagram overlap analysis were based on hypergeometric tests. Box plots were generated using ggpubr, with the horizontal center lines denoting the median and box edges denoting the interquartile range. P_{adj} were calculated by Wilcoxon signed-rank test and adjusted by holm.

Data Availability

The RNA-seq and ChIP-seq data sets can be accessed under GEO accession number GSE145190. The process files and code can be found in GitHub (https://github.com/CCLYLabBioinformatics/epigenetic-mechanism-of-PHF23).

Disclosure of Potential Conflicts of Interest

No potential conflicts of interest were disclosed.

Authors' Contributions

M. Chen: Data curation, formal analysis, investigation, visualization, methodology, writing–original draft, writing–review and editing. **X. Chen:** Data curation, formal analysis, investigation, visualization, methodology, writing–original draft, writing–review and editing. **S. Li:** Investigation. **X. Pan:** Investigation. **Y. Gong:** Investigation. **J. Zheng:** Investigation. **J. Xu:** Investigation. **C. Zhao:** Investigation. **Q. Zhang:** Investigation. **S. Zhang:** Investigation. **L. Qi:** Investigation. **Z. Wang:** Investigation. **K. Shi:** Investigation. **B.-S. Ding:** Resources. **Z. Xue:** Resources. **L. Chen:** Software. **S. Yang:** Resources. **Y. Wang:** Resources. **T. Niu:** Resources. **L. Dai:** Investigation. **S.W. Lowe:** Resources, funding acquisition. **C. Chen:** Conceptualization, resources, supervision, funding acquisition, writing–original draft, writing–review and editing. **Y. Liu:** Conceptualization, resources, supervision, funding acquisition, writing–original draft, project administration, writing–review and editing.

Acknowledgments

We thank Dr. Yuquan Wei for generous support, Dr. Junhong Han and Dr. Dan Xie for their invaluable advice and help on ChIP-seq, Dr. Yinglan Zhao, Dr. Hanshuo Yang, and Ruizhan Tong for their technical support, all the laboratory members in the Chen and Liu laboratory for their insightful advice and kind support, and the Core Facilities of West China Hospital. This work was supported by the National Key R&D Program of China (2017YFA0505600), the National Natural Science Foundation of China (81670182, 81770157, 81522003, 81570150), and the Sichuan Science and Technology Program (2020ZYD002, 2018JZ0077, 2017TJPT0005). The screening was performed at Memorial Sloan Kettering Cancer Center where it was supported by grants CA087497 and CA190261 from the National Cancer Institute and MSKCC Cancer Center support grant P30 CA008748. Scott W. Lowe is the Geoffrey Beene Chair for Cancer Biology and an investigator in the Howard Hughes Medical Institute.

The costs of publication of this article were defrayed in part by the payment of page charges. This article must therefore be hereby marked *advertisement* in accordance with 18 U.S.C. Section 1734 solely to indicate this fact.

Received March 19, 2020; revised July 19, 2020; accepted September 22, 2020; published first September 25, 2020.

REFERENCES

1. Hanahan D, Weinberg RA. Hallmarks of cancer: the next generation. Cell 2011;144:646–74.
2. Consortium ITP-CAoWG. Pan-cancer analysis of whole genomes. Nature 2020;578:82–93.

Downloaded from cancerdiscovery.aacrjournals.org on December 30, 2020. © 2020 American Association for Cancer Research.

Published OnlineFirst September 25, 2020; DOI: 10.1158/2159-8290.CD-20-0336

3. Gerstung M, Jolly C, Leshchiner I, Dentro SC, Gonzalez S, Rosebrock D, et al. The evolutionary history of 2,658 cancers. Nature 2020;578:122–8.
4. Li Y, Roberts ND, Wala JA, Shapira O, Schumacher SE, Kumar K, et al. Patterns of somatic structural variation in human cancer genomes. Nature 2020;578:112–21.
5. Zabarovsky ER, Lerman MI, Minna JD. Tumor suppressor genes on chromosome 3p involved in the pathogenesis of lung and other cancers. Oncogene 2002;21:6915–35.
6. Kallioniemi A, Kallioniemi OP, Piper J, Tanner M, Stokke T, Chen L, et al. Detection and mapping of amplified DNA sequences in breast cancer by comparative genomic hybridization. Proc Natl Acad Sci U S A 1994;91:2156–60.
7. Rodriguez MA, Ford RJ, Goodacre A, Selvanayagam P, Cabanillas F, Deisseroth AB. Chromosome 17- and p53 changes in lymphoma. Br J Haematol 1991;79:575–82.
8. Liu Y, Chen C, Xu Z, Scuoppo C, Rillahan CD, Gao J, et al. Deletions linked to TP53 loss drive cancer through p53-independent mechanisms. Nature 2016;531:471–5.
9. Reddy A, Zhang J, Davis NS, Moffitt AB, Love CL, Waldrop A, et al. Genetic and functional drivers of diffuse large B cell lymphoma. Cell 2017;171:481–94.
10. Schmitz R, Wright GW, Huang DW, Johnson CA, Phelan JD, Wang JQ, et al. Genetics and pathogenesis of diffuse large B-cell lymphoma. N Engl J Med 2018;378:1396–407.
11. Solimini NL, Xu Q, Mermel CH, Liang AC, Schlabach MR, Luo J, et al. Recurrent hemizygous deletions in cancers may optimize proliferative potential. Science 2012;337:104–9.
12. Davoli T, Xu AW, Mengwasser KE, Sack LM, Yoon JC, Park PJ, et al. Cumulative haploinsufficiency and triplosensitivity drive aneuploidy patterns and shape the cancer genome. Cell 2013;155:948–62.
13. Scuoppo C, Miething C, Lindqvist L, Reyes J, Ruse C, Appelmann I, et al. A tumour suppressor network relying on the polyamine–hypusine axis. Nature 2012;487:244–8.
14. Knudson AG Jr. Mutation and cancer: statistical study of retinoblastoma. Proc Natl Acad Sci U S A 1971;68:820–3.
15. Tavtigian SV, Simard J, Teng DH, Abtin V, Baumgard M, Beck A, et al. A candidate prostate cancer susceptibility gene at chromosome 17p. Nat Genet 2001;27:172–80.
16. Su GH, Hilgers W, Shekher MC, Tang DJ, Yeo CJ, Hruban RH, et al. Alterations in pancreatic, biliary, and breast carcinomas support MKK4 as a genetically targeted tumor suppressor gene. Cancer Res 1998;58:2339–42.
17. Reader JC, Leng Q, Rassool FV, Ning Y. Regulation of differentiation by a PHD domain in the NUP98-PHF23 fusion protein. Leuk Res 2010;34:1094–7.
18. Gough SM, Lee F, Yang F, Walker RL, Zhu YJ, Pineda M, et al. NUP98–PHF23 is a chromatin-modifying oncoprotein that causes a wide array of leukemias sensitive to inhibition of PHD histone reader function. Cancer Discov 2014;4:564–77.
19. Reader J, Meekins J, Gojo I, Ning Y. A novel NUP98-PHF23 fusion resulting from a cryptic translocation t (11; 17)(p15; p13) in acute myeloid leukemia. Leukemia 2007;21:842–4.
20. Wang GG, Song J, Wang Z, Dormann HL, Casadio F, Li H, et al. Haematopoietic malignancies caused by dysregulation of a chromatin-binding PHD finger. Nature 2009;459:847–51.
21. Nakagawa M, Tsuzuki S, Honma K, Taguchi O, Seto M. Synergistic effect of Bcl2, Myc and Ccnd1 transforms mouse primary B cells into malignant cells. Haematologica 2011;96:1318–26.
22. Adams J, Harris A, Pinkert C, Corcoran L, Alexander W, Cory S, et al. The c-myc oncogene driven by immunoglobulin enhancers induces lymphoid malignancy in transgenic mice. Nature 1985;318:533–8.
23. Kato MV, Shimizu T, Ishizaki K, Kaneko A, Yandell DW, Toguchida J, et al. Loss of heterozygosity on chromosome 17 and mutation of the p53 gene in retinoblastoma. Cancer Lett 1996;106:75–82.
24. Nigro JM, Baker SJ, Preisinger AC, Jessup JM, Hosteller R, Cleary K, et al. Mutations in the p53 gene occur in diverse human tumour types. Nature 1989;342:705–8.
25. Chen C, Liu Y, Rappaport AR, Kitzing T, Schultz N, Zhao Z, et al. MLL3 is a haploinsufficient 7q tumor suppressor in acute myeloid leukemia. Cancer Cell 2014;25:652–65.
26. McNerney ME, Brown CD, Wang X, Bartom ET, Karmakar S, Bandlamudi C, et al. CUX1 is a haploinsufficient tumor suppressor gene on chromosome 7 frequently inactivated in acute myeloid leukemia. Blood 2013;121:975–83.
27. Luo H, Li Q, O'Neal J, Kreisel F, Le Beau MM, Tomasson MH. c-Myc rapidly induces acute myeloid leukemia in mice without evidence of lymphoma-associated antiapoptotic mutations. Blood 2005;106:2452–61.
28. Ho H, Skaist AM, Pallavajjala A, Yonescu R, Batista D, Wheelan SJ, et al. NUP98-PHF23 fusion is recurrent in acute myeloid leukemia and shares gene expression signature of leukemic stem cells. Leuk Res 2016;45:1–7.
29. Warmuth M, Kim S, Gu XJ, Xia G, Adrian F. Ba/F3 cells and their use in kinase drug discovery. Curr Opin Oncol 2007;19:55–60.
30. Jenuwein T, Allis CD. Translating the histone code. Science 2001;293:1074–80.
31. Aikaterini N, Chrisavgi T, Lavigne MD, Vassiliki L, Jeroen D, Triantafillos P, et al. The dual role of LSD1 and HDAC3 in STAT5-dependent transcription is determined by protein interactions, binding affinities, motifs and genomic positions. Nucleic Acids Res 2017:45:142–54.
32. Pal R, Janz M, Galson DL, Gries M, Li S, Jöhrens K, et al. C/EBPβ regulates transcription factors critical for proliferation and survival of multiple myeloma cells. Blood 2009;114:3890–8.
33. Coerver KA, Gray SM, Barnes JE, Armstrong DL, McCabe ER. Developmental expression of hexokinase 1 and 3 in rats. Histochem Cell Biol 1998;109:75–86.
34. Grzenda A, Lomberk G, Zhang JS, Urrutia R. Sin3: master scaffold and transcriptional corepressor. Biochim Biophys Acta 2009;1789:443–50.
35. Dannenberg JH, David G, Zhong S, van der Torre J, Wong WH, Depinho RA. mSin3A corepressor regulates diverse transcriptional networks governing normal and neoplastic growth and survival. Genes Dev 2005;19:1581–95.
36. Fleischer TC, Yun UJ, Ayer DE. Identification and characterization of three new components of the mSin3A corepressor complex. Mol Cell Biol 2003;23:3456–67.
37. Zhang Y, Dufau ML. Silencing of transcription of the human luteinizing hormone receptor gene by histone deacetylase-mSin3A complex. J Biol Chem 2002;277:33431–8.
38. Pena PV, Davrazou F, Shi X, Walter KL, Verkhusha VV, Gozani O, et al. Molecular mechanism of histone H3K4me3 recognition by plant homeodomain of ING2. Nature 2006;442:100–3.
39. Shi X, Hong T, Walter KL, Ewalt M, Michishita E, Hung T, et al. ING2 PHD domain links histone H3 lysine 4 methylation to active gene repression. Nature 2006;442:96–9.
40. Kuzmichev A, Zhang Y, Erdjument-Bromage H, Tempst P, Reinberg D. Role of the Sin3-histone deacetylase complex in growth regulation by the candidate tumor suppressor p33(ING1). Mol Cell Biol 2002;22:835–48.
41. Roadmap Epigenomics C, Kundaje A, Meuleman W, Ernst J, Bilenky M, Yen A, et al. Integrative analysis of 111 reference human epigenomes. Nature 2015;518:317–30.
42. Liberzon A, Birger C, Thorvaldsdottir H, Ghandi M, Mesirov JP, Tamayo P. The Molecular Signatures Database (MSigDB) hallmark gene set collection. Cell Syst 2015;1:417–25.
43. Heideman MR, Lancini C, Proost N, Yanover E, Jacobs H, Dannenberg J-H. Sin3a-associated Hdac1 and Hdac2 are essential for hematopoietic stem cell homeostasis and contribute differentially to hematopoiesis. Haematologica 2014;99:1292–303.
44. Wang H, Yang H, Shivalila CS, Dawlaty MM, Cheng AW, Zhang F, et al. One-step generation of mice carrying mutations in multiple genes by CRISPR/Cas-mediated genome engineering. Cell 2013;153:910–8.
45. Lee MG, Villa R, Trojer P, Norman J, Yan KP, Reinberg D, et al. Demethylation of H3K27 regulates polycomb recruitment and H2A ubiquitination. Science 2007;318:447–50.
46. Gifford CA, Ziller MJ, Gu H, Trapnell C, Donaghey J, Tsankov A, et al. Transcriptional and epigenetic dynamics during specification of human embryonic stem cells. Cell 2013;153:1149–63.
47. Ramírez F, Ryan DP, Grüning B, Bhardwaj V, Kilpert F, Richter AS, et al. deepTools2: a next generation web server for deep-sequencing data analysis. Nucleic Acids Res 2016;44:W160–W5.

Downloaded from cancerdiscovery.aacrjournals.org on December 30, 2020. © 2020 American Association for Cancer Research.

Published OnlineFirst September 25, 2020; DOI: 10.1158/2159-8290.CD-20-0336

AACR American Association for Cancer Research

CANCER DISCOVERY

An Epigenetic Mechanism Underlying Chromosome 17p Deletion–Driven Tumorigenesis

Mei Chen, Xuelan Chen, Shujun Li, et al.

Cancer Discov Published OnlineFirst September 25, 2020.

Updated version	Access the most recent version of this article at: doi:10.1158/2159-8290.CD-20-0336
Supplementary Material	Access the most recent supplemental material at: http://cancerdiscovery.aacrjournals.org/content/suppl/2020/09/25/2159-8290.CD-20-0336.DC1

E-mail alerts	Sign up to receive free email-alerts related to this article or journal.
Reprints and Subscriptions	To order reprints of this article or to subscribe to the journal, contact the AACR Publications Department at pubs@aacr.org.
Permissions	To request permission to re-use all or part of this article, use this link http://cancerdiscovery.aacrjournals.org/content/early/2020/12/18/2159-8290.CD-20-0336. Click on "Request Permissions" which will take you to the Copyright Clearance Center's (CCC) Rightslink site.

Downloaded from cancerdiscovery.aacrjournals.org on December 30, 2020. © 2020 American Association for Cancer Research.